SIAM J. APPL. MATH.
Vol. 75, No. 3, pp. 978–998

MULTILUMP SYMMETRIC AND NONSYMMETRIC GRAVITY-CAPILLARY SOLITARY WAVES IN DEEP WATER*

ZHAN WANG† AND JEAN-MARC VANDEN-BROECK‡

Abstract. Multilump gravity-capillary solitary waves propagating in a fluid of infinite depth are computed numerically. The study is based on a weakly nonlinear and dispersive partial differential equation (PDE) with weak variations in the spanwise direction, a model derived by Akers and Milewski [*Stud. Appl. Math.*, 122 (2009), pp. 249–274]. For a two-dimensional fluid, this model agrees qualitatively well with the full Euler equations for the bifurcation curves, wave profiles, and dynamics of solitary waves. Fully localized solitary waves are then computed for three-dimensional fluids. New symmetric lump solutions are computed by using a continuation method to follow the branch of elevation waves. It is then found that the branch of elevation waves has multiple turning points from which new solutions, consisting of multiple lumps separated by smaller oscillations, bifurcate. Nonsymmetric solitary waves, which also feature a multilump structure, are computed and found to appear via spontaneous symmetry-breaking bifurcations. It is shown that all these new steady solutions are unstable to either longitudinal or transverse perturbations and that the moderate-amplitude depression solitary waves and the linear dispersive waves serve as attractors in the long-time evolution of the instability.

Key words. water wave, gravity-capillary free-surface flows, multilump solitary waves, nonsymmetric solitary waves

AMS subject classifications. 15A15, 15A09, 15A23

DOI. 10.1137/140992941

1. Introduction.

Gravity-capillary waves, which are commonly referred to as wind ripples, are ubiquitous on the wind-swept surface of fluids. These waves have attracted growing interest since they enjoy wide usage in microwave radar remote sensing (because the typical wavelength of gravity-capillary waves and that of the microwave radiation emitted from the scatterometer radar are similar [24, 26]). They are also used to test the prediction of weak turbulence [9]. Furthermore these waves can overturn and trap air bubbles due to the geometric nature of the surface tension effect [11, 21]; hence they may contribute to the underwater acoustic background [16]. Due to those physical significances, in-depth knowledge of the characteristics of gravity-capillary waves is therefore essential.

We shall consider gravity-capillary waves in deep water with the effects of viscosity neglected. In particular we shall concentrate on a recently discovered type of solitary waves which bifurcate from infinitesimal periodic waves at the minimum of the linear phase speed where the group velocity is equal to the phase velocity, and which are characterized by oscillatory decaying tails. In the small-amplitude limit, the envelopes of these solitary waves are well described by the soliton solution of the focusing cubic nonlinear Schrödinger equation (NLS) and are thereby called wavepacket solitary waves [7].

*Received by the editors October 24, 2014; accepted for publication (in revised form) March 3, 2015; published electronically May 14, 2015. This work was partially supported by EPSRC under grant EP/J019569/1.

http://www.siam.org/journals/siap/75-3/99294.html

†Department of Mathematical Sciences, University of Bath, Claverton Down, Bath BA2 7AY, UK, and Department of Mathematics, University College London, London WC1E 6BT, UK (z.wang5@bath.ac.uk).

‡Department of Mathematics, University College London, London WC1E 6BT, UK (j.vanden-broeck@ucl.ac.uk).

The computations of these gravity-capillary solitary waves in a two-dimensional (2D) fluid of infinite depth (corresponding to a one-dimensional (1D) free surface) were pioneered by Longuet-Higgins [12]. He computed a branch of waves called depression solitary waves (the midpoints of these waves lie below the mean water level) from the full Euler equations. They are characterized by a monotonic speed-amplitude relation. Later, Vanden-Broeck and Dias [20] found another branch of solitary waves with a positive free-surface elevation at the center, which were thereafter called elevation solitary waves. In contrast to the branch of depression waves, there are turning points on the branch of the elevation waves [8] at which multimodal solutions, consisting of several humps separated by smaller oscillations, bifurcate (see [8] or Figure 1(a)). These two basic branches both correspond to symmetric solitary waves. However, recent computation [23] with the full Euler equations shows that nonsymmetric gravity-capillary solitary waves also exist in deep water. These asymmetric waves have a multimodal structure and appear via spontaneous symmetry-breaking bifurcations. These results are consistent with earlier computations by Zufiria [27] and with the asymptotic analysis of Yang and Akylas [25] based on the fifth-order Korteweg–de Vries equation, a model for gravity-capillary waves propagating in 2D fluids of finite depth when the Bond number $B = \sigma/\rho g h^2$ (σ is the surface tension coefficient, ρ is the fluid density, g is the gravitational acceleration and h is mean depth of the fluid) is close to $1/3$.

In contrast to the pure gravity solitary waves which exist only in 2D fluids (see the rigorous proof in Craig [6]) and in the shallow water regime, the gravity-capillary solitary waves can exist for both two- and three-dimensional fluids of arbitrary depth. For a three-dimensional fluid domain (with a 2D free surface), the first computation of "lump" solutions, which were locally confined in all spatial directions, was by Părău, Vanden-Broeck, and Cooker [15], with related work by Kim and Akylas [13] and Milewski [17] on reduced models. Both elevation and depression lumps were found. They are traveling wavepackets whose envelopes are governed by the ground state of 2+1 focusing cubic NLS in the small-amplitude limit. The new findings in 2D fluids, such as the snakelike bifurcation of the elevation branch and the existence of nonsymmetric solitary waves (see previous paragraph), naturally bring up the question of the possible existence of similar phenomena in the three-dimensional case. This is the main problem that we address in the present paper.

Akers and Milewski [1] proposed a Kadomtsev–Petviashvili type model for gravity-capillary waves in deep water. With this model, these authors reproduced basic elevation and depression lumps and investigated their dynamics, including the transverse instability of plane solitary waves, the stability characteristics of lumps, and different kinds of collisions. Later, Cho et al. [5] generalized this model to involve forcing and dissipation to study the generation of lumps by moving an air source with the speed slightly below the phase speed minimum. The comparison between their numerical results and experimental observations shows good qualitative agreement [3, 4].

In this paper the Akers–Milewski model is used to compute new elevation lumps and nonsymmetric lumps in deep water, both of which feature a superposition of multiple lumps (these waves are henceforth called multilump gravity-capillary waves, a name inherited from the NLS).

The rest of the paper is structured as follows. For completeness we briefly describe the derivation of the Akers–Milewski equation in section 2. The multilump elevation

solitary waves and the nonsymmetric solutions are presented in section 3, as well as their bifurcation mechanism, which is elucidated from two different points of view. Finally the stability characteristics of these new waves are carried out via the numerical time integration of the model equation.

2. Formulation.

2.1. Mathematical description. We consider a three-dimensional, incompressible, and inviscid fluid flowing irrotationally. Let (x, y) denote the horizontal coordinates, z the vertical direction with $z = 0$ at the undisturbed interface between fluid and vacuum, and t the time. The fluid is supposed to be infinitely deep with a free surface $z = \eta(x, y, t)$ on the top. For irrotational flow there exists a potential function ϕ such that the velocity field of the fluid can be expressed as (ϕ_x, ϕ_y, ϕ_z). Therefore the study of an irrotational flow reduces to the problem of determining ϕ, which satisfies Laplace equation in the fluid domain

$$\phi_{xx} + \phi_{yy} + \phi_{zz} = 0 \qquad \text{for } z < \eta(x, y, t). \tag{2.1}$$

On the free surface $z = \eta(x, y, t)$, the kinematic and dynamic boundary conditions need to be satisfied:

$$\eta_t = \phi_z - \nabla\eta \cdot \nabla\phi\,, \tag{2.2}$$

$$\phi_t = -\frac{1}{2}\left(|\nabla\phi|^2 + \phi_z^2\right) - g\eta + \frac{\sigma}{\rho}\nabla \cdot \left[\frac{\nabla\eta}{\sqrt{1 + |\nabla\eta|^2}}\right], \tag{2.3}$$

where ∇ and $\nabla\cdot$ are the gradient and the divergent operators acting in the horizontal variables, g is the acceleration of gravity, σ represents the surface tension coefficient, and ρ is the density of the fluid. Since gravity and surface tension are equally important for our problem, we can nondimensionalize the system by choosing

$$\left[\frac{\sigma}{\rho g}\right]^{1/2}, \qquad \left[\frac{\sigma}{\rho g^3}\right]^{1/4}, \qquad \left[\frac{\sigma g}{\rho}\right]^{1/4} \tag{2.4}$$

as length, time, and potential scales, respectively. Therefore, the dynamic boundary condition (2.3) can be reduced to

$$\phi_t = -\frac{1}{2}\left(|\nabla\phi|^2 + \phi_z^2\right) - \eta + \nabla \cdot \left[\frac{\nabla\eta}{\sqrt{1 + |\nabla\eta|^2}}\right]. \tag{2.5}$$

Finally, the boundary condition at infinity

$$\phi_z \to 0 \qquad \text{as } z \to -\infty \tag{2.6}$$

completes the whole system.

2.2. Akers–Milewski model. In order to simplify the numerical computations of the full Euler system (2.1)–(2.6) while capturing the essential dynamic properties, Akers and Milewski [1] proposed a simple one-way model for gravity-capillary waves in deep water. The Akers–Milewski model was generalized by Cho et al. [5] by adding forcing and dissipation to investigate the wave pattern generated by a pressure source moving over the free surface at speeds slightly below the resonant speed. They showed

that results from both laboratory experiments (Diorio et al. [3, 4]) and numerical simulations (Cho et al. [5]) were in good agreement.

For completeness, in what follows we give a brief description of the derivation of the Akers–Milewski model. The dispersion relation or, equivalently, the phase speed c_p is given by the solutions to the linearization of (2.1), (2.2), (2.5), and (2.6) about a quiescent state and is

$$\omega^2 = \sqrt{k^2+l^2}\,\Big(1+k^2+l^2\Big), \quad |c_p|^2 = \frac{1}{\sqrt{k^2+l^2}}\Big(1+k^2+l^2\Big), \tag{2.7}$$

where ω is the frequency of linear waves, k and l represent the wavenumber in the x- and y-directions, respectively, and c_p denotes the phase velocity. We assume that waves propagate in the x-direction only, and as a consequence, y is the spanwise direction (the direction transverse to the wave propagation). It follows that the phase speed $|c_p|$ attains its minimum $\sqrt{2}$ at $k=\pm 1$ and $l=0$. For the right-going waves,

$$\omega = \operatorname{sgn}(k)\,\sqrt{(k^2+l^2)^{1/2}+(k^2+l^2)^{3/2}}. \tag{2.8}$$

Following Akers and Milewski [1], the model is supposed to be valid in the vicinity of unidirectional traveling waves with the wavenumber $(\pm 1, 0)$. Therefore ω can be approximated by the second-order truncation of its Taylor series about the point $(|k^*|, l^*) = (1,0)$ and it takes the form

$$\omega \approx \frac{\sqrt{2}}{4}\operatorname{sgn}(k)\Big(1+2|k|+k^2+2l^2\Big) \triangleq \widetilde{\omega}. \tag{2.9}$$

By substituting $i\partial_t$ for ω, $-i\partial_x$ for k, $-i\partial_y$ for l, and $i\mathcal{H}$ for $\operatorname{sgn}(k)$ in the approximation (2.9), one obtains the linear dispersive equation

$$\eta_t + \frac{\sqrt{2}}{2}\,\eta_x - \frac{\sqrt{2}}{4}\,\mathcal{H}\Big[\eta - \eta_{xx} - 2\eta_{yy}\Big] = 0. \tag{2.10}$$

Here $\mathcal{H}$ is the Hilbert transform with respect to x, whose Fourier symbol is $-i\operatorname{sgn}(k)$. To complete the equation, the Burgers' type nonlinearity is added to (2.10). Finally we arrive at

$$\eta_t + \frac{\sqrt{2}}{2}\,\eta_x - \frac{\sqrt{2}}{4}\,\mathcal{H}\Big[\eta - \eta_{xx} - 2\eta_{yy}\Big] + \alpha\left(\eta^2\right)_x = 0\,. \tag{2.11}$$

Following Akers and Milewski [1], the constant α can be obtained by matching with the nonlinear coefficient of the underlying cubic NLS of the full Euler equations. The NLS is a conventional tool for studying the dynamics of the small-amplitude modulated wavepackets of (2.11). Briefly we introduce the amplitude parameter ϵ and the slow-varying variables $(X,Y,T,\tau) = (\epsilon x, \epsilon y, \epsilon t, \epsilon^2 t)$, then expand the free surface as

$$\eta = \epsilon A(X - c_g T, Y, \tau)e^{i\theta} + \epsilon^2 A_2(X - c_g T, Y, \tau)e^{2i\theta} + \text{c.c.} + \cdots, \tag{2.12}$$

where c.c. represents the complex conjugate, $\theta = kx + ly - \widetilde{\omega}t$ with $k=\pm 1$ and $l=0$, and $c_g = \partial_k \widetilde{\omega} = \frac{\sqrt{2}}{2}(1+|k|)$. We substitute the ansatz (2.12) into (2.11) and equate like powers of ϵ. It turns out that the envelope A is governed by the NLS

$$iA_\tau + \frac{\sqrt{2}}{4}A_{XX} + \frac{\sqrt{2}}{2}A_{YY} + 8\sqrt{2}\alpha^2|A|^2A = 0. \tag{2.13}$$

Since the coefficient of the cubic nonlinearity is $11\sqrt{2}/8$ for the full Euler equations (see [1, 5, 22], for example), it follows that

$$8\sqrt{2}\,\alpha^2 = \frac{11}{8}\sqrt{2} \implies \alpha = \frac{\sqrt{11}}{8}\,. \tag{2.14}$$

It is easy to prove that (2.11) conserves

$$\int\int_{\mathbb{R}^2} \eta \; dxdy, \qquad \int\int_{\mathbb{R}^2} \eta^2 \; dxdy \tag{2.15}$$

corresponding to the conservation of mass and the conservation of energy, respectively. Furthermore, this equation has a Hamiltonian structure, as it can be written as $\eta_t = \partial_x \left(\delta \mathcal{J}/\delta\eta\right)$ with the Hamiltonian functional

$$\mathcal{J}[\eta] = \int\int_{\mathbb{R}^2} \left[-\frac{\sqrt{2}}{4}\eta^2 + \frac{\sqrt{2}}{8}\eta\,\mathcal{H}\partial_x^{-1}\Big[\eta - \eta_{xx} - 2\eta_{yy}\Big] - \frac{\sqrt{11}}{24}\eta^3 \right] dxdy. \tag{2.16}$$

For traveling waves, we assume $\eta(x, y, t) = \eta(x - ct, y)$, where the constant c is called the translating speed. Hence the governing equation takes the form

$$\left(\frac{\sqrt{2}}{2} - c\right)\,\eta_x - \frac{\sqrt{2}}{4}\,\mathcal{H}\Big[\eta - \eta_{xx} - 2\eta_{yy}\Big] + \frac{\sqrt{11}}{8}\left(\eta^2\right)_x = 0\,. \tag{2.17}$$

In the next section fully localized traveling-wave solutions are obtained from the model (2.17) for both 1D and 2D problems. We should clarify that "1D wave" or "1D problem" or "plane wave" refers to the case when (2.11) is independent of the variable y, and as a consequence, "2D wave" or "2D problem" means η depends on both x and y in space.

3. Results.

3.1. Model validation. The speed-amplitude (where "amplitude" is defined as the elevation of the center of the free surface) bifurcation diagram for 1D gravity-capillary solitary waves of the full Euler equations in deep water was obtained by Vanden-Broeck and Dias [20] and then extended by Dias, Menasce, and Vanden-Broeck [8]. These authors found that the branch of elevation waves has multiple turning points. In Figure 1(a), we compare the speed-amplitude bifurcation curves of the reduced model (2.17) (solid line), the full Euler equations (dashed line), and the leading order of the NLS prediction (dash-dotted line) for the branch of elevation. The first turning point A occurs at $c \approx 1.22$ for the reduced model, which is slightly different from that of the full Euler equations. The second turning point B ($c \approx 1.407$) appears close to the bifurcation point (i.e., the phase speed minimum). The wave profiles resemble two depression waves placed side-by-side after the first turning point A (a typical profile is shown in Figure 2(a)) and feature two single-hump elevation waves separated by small oscillations when the second turning point B is passed (see Figure 2(b)). We stop the computation after passing through the second turning point. It is not clear whether the model equation (2.17) has the third turning point since at the stopping point the computation time becomes prohibitive in order to achieved the desired accuracy, while the full Euler equations do have more turning points [8, 23]. The comparison of typical wave profiles between the model (2.17) (solid lines) and the full Euler equations (dashed lines) is made in Figure 2. It is clear that

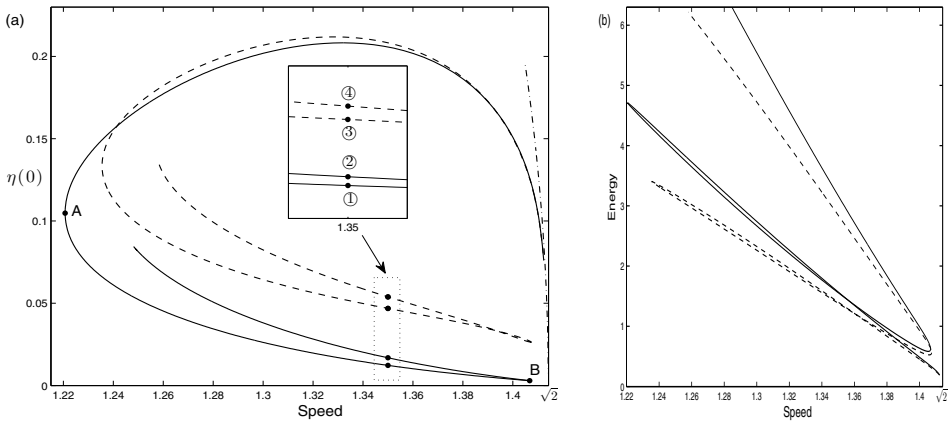

FIG. 1. (a) 1*D elevation branch computed using the model equation (solid line) and the full Euler equations (dashed line), together with the small amplitude asymptotic prediction (dash-dotted curve, calculated using the* 1*D NLS). The branch, which is parameterized by the value of* η *at the middle point of solitary waves, features multiple turning points (labeled* A *and* B*). The wave profiles for the points* ①–④ *are shown in Figure* 2. (b) *Speed-energy bifurcation curves for the model equation using rescaled* L^2*-norm (solid line) and the full Euler equations (dashed line).*

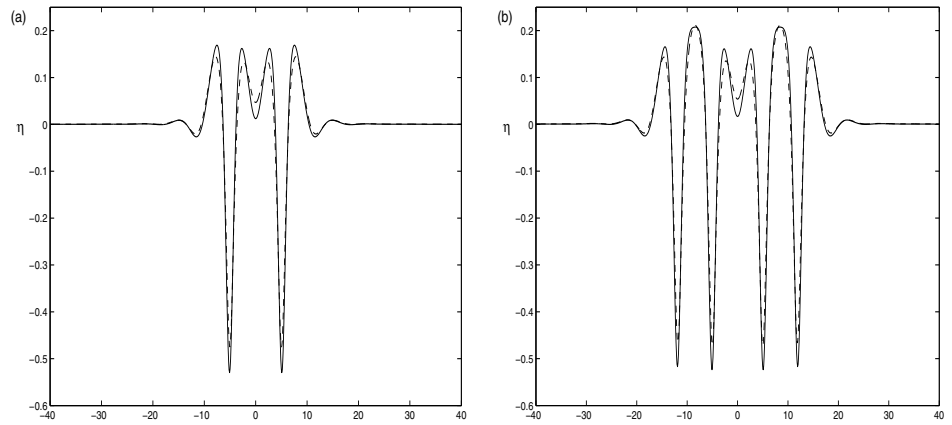

FIG. 2. *Typical profiles of elevation solitary waves at* $c = 1.35$*, computed by the model equation (solid lines) and the Euler equations (dashed lines).* (a) *Profiles correspond to* ① *and* ③ *in Figure* 1(a). (b) *Profiles correspond to* ② *and* ④ *in Figure* 1(a).

the solutions of the model equation overpredict the peak amplitudes of the full Euler solutions, but the model is remarkably accurate in a qualitative sense. It is noted that (2.17) was solved via the classic pseudospectral method in the Fourier space (see [1] for the details). The numerical method for the full steady Euler equations is provided in detail in the appendix (readers are also referred to [18, 23] for more information).

In Figure 1(b) we compare the speed-energy bifurcation curves of the reduced model (solid line) and the full Euler equations (dashed line) for the branch of elevation

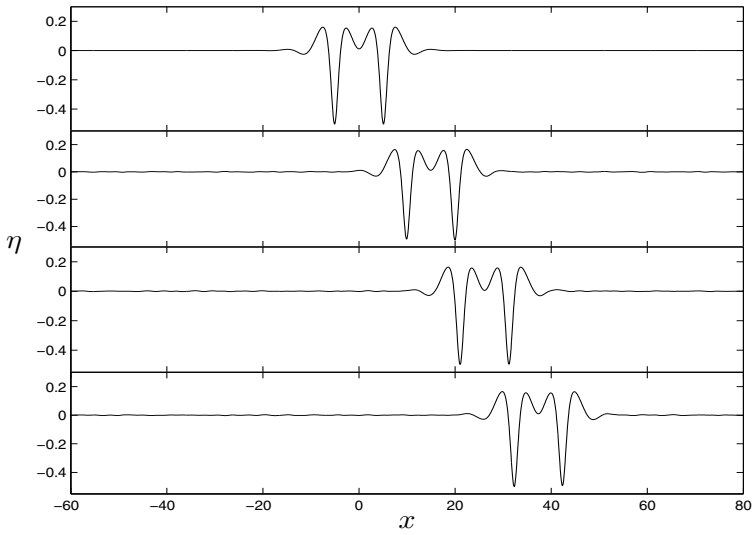

FIG. 3. *Evolution of* 1*D stable elevation solitary waves for the model equation. The undisturbed wave is shown as a solid line in Figure* 2(a). *Four free-surface profiles are shown in the dynamics of a perturbed (*5% *negative energy perturbation) elevation wave:* $t = 0, 2000, 3500, 5000$ *from top to bottom. The profiles are shown in a frame of reference moving to the right with the speed* $c = 1.35$.

solitary waves. The total energy of the full Euler equations can be expressed as

$$\mathcal{E} = \frac{1}{2}\int_{\mathbb{R}}\int_{-\infty}^{\eta}\left(\phi_x^2+\phi_z^2\right)\,dzdx + \frac{1}{2}\int_{\mathbb{R}}\eta^2\,dx + \int_{\mathbb{R}}\left(\sqrt{1+\eta_x^2}-1\right)\,dx\,. \tag{3.1}$$

For the reduced model, (3.1) can be approximated by

$$\mathcal{E} \;\approx\; 2\int_{\mathbb{R}}\eta^2\,dx, \tag{3.2}$$

recalling that the model is valid in the vicinity of unidirectional waves near wavenumber $(\pm 1, 0)$. Even though these two curves are quantitatively different, the qualitative property is the same: the segments between two successive turning points are monotonically decreasing. This fact is closely related to the transverse instability of plane solitary waves, and we will elaborate on this in the next section.

The longitudinal stability of 1D gravity-capillary solitary waves for the full Euler equations was investigated by Calvo and Akylas [2] based on a numerical eigenvalue analysis. They concluded that the depression solitary waves are stable both in the small-amplitude limit and at finite steepness. On the other hand, the elevation waves are unstable at small amplitudes but regain spectral stability as the first turning point is passed. These results were confirmed recently by Milewski, Vanden-Broeck, and Wang [18] via direct numerical simulations of the full Euler equations.

We now show that the same results can be obtained for the model equation (2.11). The stability of depression waves and the instability of small-amplitude elevation waves were shown in [1]. Between the turning points A and B in Figure 1(a), a variety of perturbations with 5% of the energy of the initial waves did not show instability. This agrees well with the solutions of the Euler equations. In Figure 3, a sample time-dependent computation is shown. Note that the 5% negative energy

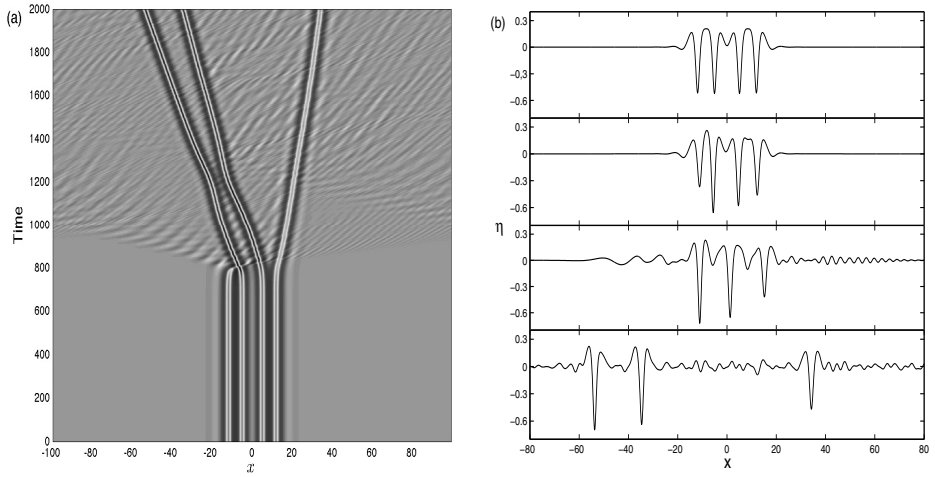

FIG. 4. *Evolution of* 1*D unstable elevation solitary waves. The initial wave profile resembles two elevation waves placed side-by-side (see the top figure in the right panel), and it finally evolves into three separated depression waves. The solution in the* $t - x$ *plane is shown in* (a)*, while the typical profiles are shown in* (b) *for* $t = 0, 780, 900, 2000$ *from top to bottom. All the figures are shown in a frame of reference moving to the right with the speed* $c = 1.35$*.*

perturbation generates a wave of slightly higher speed than the unperturbed one. Since Calvo and Akylas [2] did not consider the stability characteristics after the second turning point, we performed numerical computations in this regime with the model equation. This shows that the elevation solitary waves are again unstable. In this case all perturbations triggered rapid instabilities, and one example is presented in Figure 4. In contrast to the single-hump elevation wave (solutions before the first turning point) which finally evolves into one big trough with a lot of radiations, the traveling-wave solution featuring two humps connected by a small dimple is disturbed by numerical noise, and the structure eventually breaks up into several depression waves of different amplitudes as time evolves.

The comparison with the full Euler equations for 2D small- and moderate-amplitude depression lumps was already done in [5], while it is still not available for the branch of elevation lumps since its full bifurcation diagram for the full Euler equations is unclear.

Finally we can draw the conclusion from the bifurcation diagrams (Figure 1), the typical profiles (Figure 2), and the stability characteristics (Figures 3 and 4) that (2.11) is a qualitatively accurate model for gravity-capillary waves in deep water. In the rest of the paper, we focus on the wave patterns and their dynamics in two spatial dimensions based on the model equation (2.11).

3.2. Transverse instability. The transverse instability of plane gravity-capillary solitary waves (1D solitary waves trivially extended in the spanwise direction) is related to the eventual existence of lumps. Relevant researchers include Kim and Akylas [14], who applied variational arguments to the full Euler equations; Akers and Milewski [1], who used an analysis based on NLS and direct numerical simulations for the model (2.11); and Wang and Milewski [22], who performed numerical experiments for a quantitatively accurate model. All these studies are for 1D depression waves. As

shown in section 3.1 the elevation waves between the first and second turning points are also stable subject to longitudinal perturbations, so it is natural to inquire about their stability with respect to transverse perturbations.

We suppose $U(\theta;c)$ is a plane solitary-wave solution to (2.17) characterized by the translating speed c, where $\theta = x - ct$; it then follows that

$$\left(\frac{\sqrt{2}}{2} - c\right) U_\theta - \frac{\sqrt{2}}{4}\,\mathcal{H}\Big[U - U_{\theta\theta}\Big] + \frac{\sqrt{11}}{8}\Big(U^2\Big)_\theta = 0\,. \tag{3.3}$$

Taking the derivative with respect to c yields

$$\left(\frac{\sqrt{2}}{2} - c\right) (U_c)_\theta - \frac{\sqrt{2}}{4}\,\mathcal{H}\Big[U_c - (U_c)_{\theta\theta}\Big] + \frac{\sqrt{11}}{4}\Big(UU_c\Big)_\theta = U_\theta\,. \tag{3.4}$$

We perturb the solution in the transverse direction using a long cosine wave, namely, $\eta = U(\theta;c) + \widetilde{\eta}(\theta;c)\; e^{i\beta y + \lambda t}$ with the small wavenumber β in the direction transverse to the wave propagation. By substituting the expression for η into (2.11) and collecting the coefficient of the term $e^{i\beta y+\lambda t}$, we obtain

$$\left(\frac{\sqrt{2}}{2} - c\right) \widetilde{\eta}_\theta - \frac{\sqrt{2}}{4}\,\mathcal{H}\Big[\widetilde{\eta} - \widetilde{\eta}_{\theta\theta} + 2\beta^2\widetilde{\eta}\Big] + \frac{\sqrt{11}}{4}\Big(U\widetilde{\eta}\Big)_\theta = -\lambda\widetilde{\eta}\,. \tag{3.5}$$

Furthermore, we assume

$$\widetilde{\eta} = \eta^{(0)} + \beta\eta^{(1)} + \beta^2\eta^{(2)} + \cdots\,, \quad \lambda = \beta\lambda^{(1)} + \beta^2\lambda^{(2)} + \cdots\,. \tag{3.6}$$

By substituting the expansion (3.6) into (3.5) and equating like powers of β, we obtain at $O(1)$

$$\left(\frac{\sqrt{2}}{2} - c\right) \eta^{(0)}_\theta - \frac{\sqrt{2}}{4}\,\mathcal{H}\Big[\eta^{(0)} - \eta^{(0)}_{\theta\theta}\Big] + \frac{\sqrt{11}}{4}\Big(U\eta^{(0)}\Big)_\theta = 0\,. \tag{3.7}$$

It is obvious that $\eta^{(0)} = U_\theta$ is a solution to the homogeneous equation (3.7). To $O(\beta)$, $\eta^{(1)}$ satisfies the forced problem

$$\left(\frac{\sqrt{2}}{2} - c\right) \eta^{(1)}_\theta - \frac{\sqrt{2}}{4}\,\mathcal{H}\Big[\eta^{(1)} - \eta^{(1)}_{\theta\theta}\Big] + \frac{\sqrt{11}}{4}\Big(U\eta^{(1)}\Big)_\theta = -\lambda^{(1)}U_\theta\,. \tag{3.8}$$

Recalling (3.4), the solution to (3.8) is $\eta^{(1)} = -\lambda^{(1)}U_c$. It is a well-behaved solution. At the next order the equation for $\eta^{(2)}$ is

$$\begin{aligned}&\left(\frac{\sqrt{2}}{2} - c\right) \eta^{(2)}_\theta - \frac{\sqrt{2}}{4}\,\mathcal{H}\Big[\eta^{(2)} - \eta^{(2)}_{\theta\theta}\Big] + \frac{\sqrt{11}}{4}\Big(U\eta^{(2)}\Big)_\theta \\ &\quad = -\Big(\lambda^{(1)}\eta^{(1)} + \lambda^{(2)}\eta^{(0)}\Big) + \frac{\sqrt{2}}{2}\,\mathcal{H}\Big[\eta^{(0)}\Big]\,.\end{aligned} \tag{3.9}$$

The adjoint of the operator on the left-hand side of (3.9) is

$$\mathcal{L}^\dagger = \left(c - \frac{\sqrt{2}}{2}\right)\partial_\theta + \frac{\sqrt{2}}{4}\,\mathcal{H}\Big[1 - \partial_{\theta\theta}\Big] - \frac{\sqrt{11}}{4}U\partial_\theta \tag{3.10}$$

and it is obvious that $\mathcal{L}^{\dagger}U = 0$. It follows that the solvability condition for the inhomogeneous equation (3.9) is

$$\int_{-\infty}^{\infty} \left[-\left(\lambda^{(1)}\eta^{(1)} + \lambda^{(2)}\eta^{(0)}\right) + \frac{\sqrt{2}}{2}\mathcal{H}\left[\eta^{(0)}\right] \right] U \, d\theta = 0$$

$$\Longrightarrow \int_{-\infty}^{\infty} \left[\left(\lambda^{(1)}\right)^2 U_c U - \lambda^{(2)} U_\theta U + \frac{\sqrt{2}}{2}\mathcal{H}\left[U_\theta\right] U \right] d\theta = 0$$

$$\Longrightarrow \left(\lambda^{(1)}\right)^2 \frac{\mathrm{d}}{\mathrm{dc}} \int_{-\infty}^{\infty} U^2 d\theta = -\sqrt{2} \int_{-\infty}^{\infty} \mathcal{H}\left[U_\theta\right] U d\theta = -\sqrt{2} \int_{-\infty}^{\infty} |k| \left|\widehat{U}\right|^2 dk, \tag{3.11}$$

where the hat symbol represents the Fourier transform. It is noted that the last equality comes from the Parseval's theorem or the convolution theorem and indicates that the right-hand side of (3.11) is negative. We infer from (3.11) that the plane solitary-wave solution U is transversely unstable if it satisfies

$$\frac{\mathrm{d}}{\mathrm{dc}} \int_{-\infty}^{\infty} U^2 \, d\theta < 0 \,. \tag{3.12}$$

For elevation solitary waves, Figure 1(b) shows that (3.12) is satisfied, and hence the instability persists.

The transverse instability is investigated through direct numerical computations of the Akers–Milewski model. Snapshots of the evolution of a 1D longitudinally stable elevation wave subject to a transverse perturbation are shown in Figure 5. We take the initial condition as

$$\eta(x, y, 0) = \left[1 + 0.01 \cos\left(\frac{\pi y}{40}\right)\right] U(x), \tag{3.13}$$

where the line solitary wave U is the solution shown as a solid line in Figure 2(a). The evolution of the instability initially shows a focusing behavior and ultimately results in multiple depression lumps and a radiated wave field. We should emphasize that the transverse instability strongly suggests that fully localized depression lumps are (neutrally) stable and appear to be attractors in the long time evolution of the problem.

3.3. Bifurcation of multilump solitary waves. We now turn our attention to 2D gravity-capillary lumps. The basic elevation and depression lumps, which are symmetric in both the x and y directions, were computed in deep water with the full Euler equations by Părău, Vanden-Broeck, and Cooker [15]. These two branches bifurcate from infinitesimal periodic waves at the minimum of the linear dispersion relation where the phase velocity is aligned with the group velocity. However, the snakelike bifurcation diagram for the 1D elevation branch stimulates further investigation of the 2D elevation lumps.

The branch of elevation lumps is followed to the regime far away from the bifurcation point at infinitesimal amplitude. The bifurcation diagrams are shown in Figure 6(a) and (b) using the energy and the value of the central point of the profile as parameters. Both plots exhibit multiple turning points, which have already been observed in the 1D case. The 2D lumps were computed using at least 400×100 grid points along the propagating and spanwise directions, respectively. The solutions close to the bifurcation point are often difficult to compute accurately since the spatial

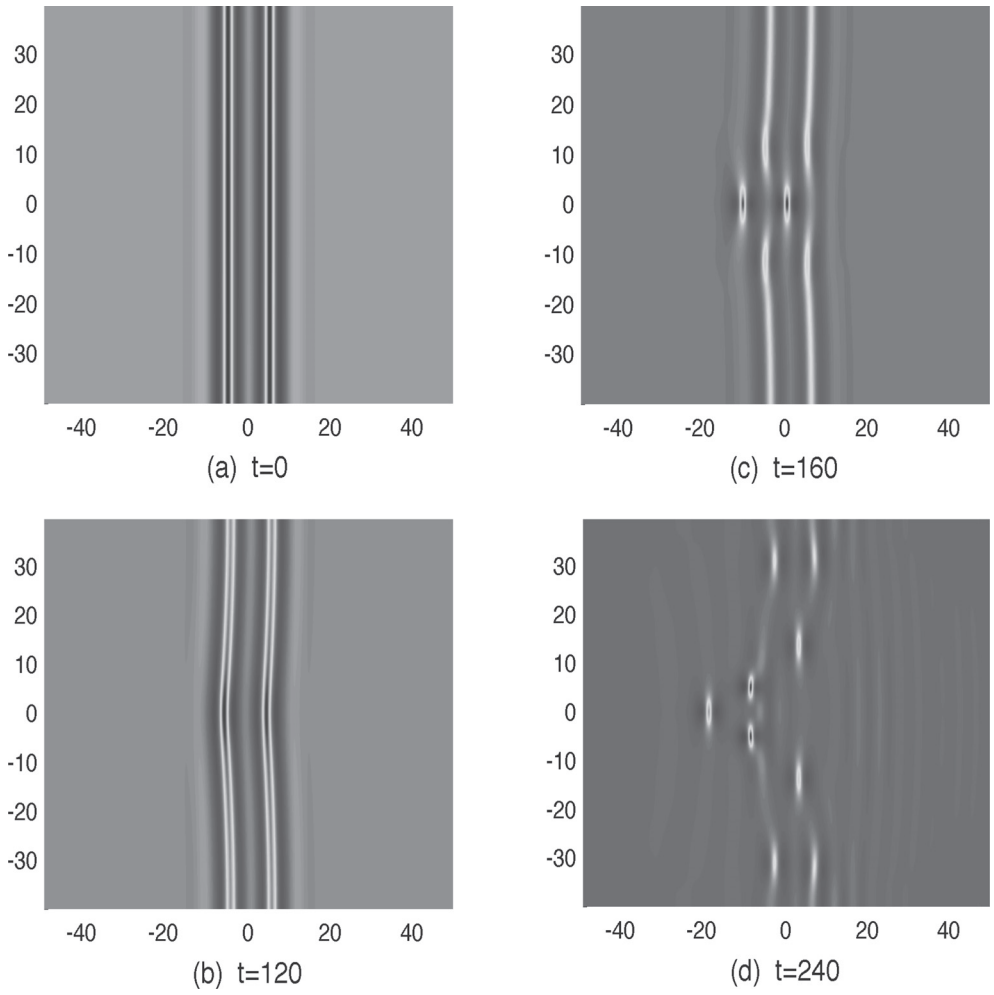

FIG. 5. *Transverse instability of the plane solitary wave. The transverse perturbation is obtained by taking the initial data as* $\eta(x, y, 0) = [1 + \epsilon \cos(\beta y)]\, U(x)$, *where* $\epsilon = 0.01$, $\beta = \pi/40$, *and* U *is the* $1D$ *traveling wave shown as a solid line in Figure* 2(a). *Evolution of the transverse instability to multiple lumps is shown for* (a) $t = 0$, (b) $t = 120$, (c) $t = 160$, *and* (d) $t = 240$.

decay of those solutions is much slower. Thus, the computational domain is gradually enlarged as the translating speed c increases. At the turning points the parameter along the curve had to be changed, and we alternated between using $\eta(0, 0)$ and c in order to follow the curve. The speed-energy curve starts from the bifurcation point $c = \sqrt{2}$, then follows the path C→D→⑤→⑥→⑦→E→⑧→F→⑨. Typical profiles corresponding to the points labeled ⑥ and ⑨ are shown in Figure 7, and both feature a multilump structure. Like in the 1D case, Figure 7(a) (corresponding to ⑥) resembles two depression lumps, while Figure 7(b) (corresponding to ⑨) is composed by two elevation lumps (four troughs). The profile ⑨ has approximately twice the energy of ⑥, since it has twice the number of troughs of similar amplitude.

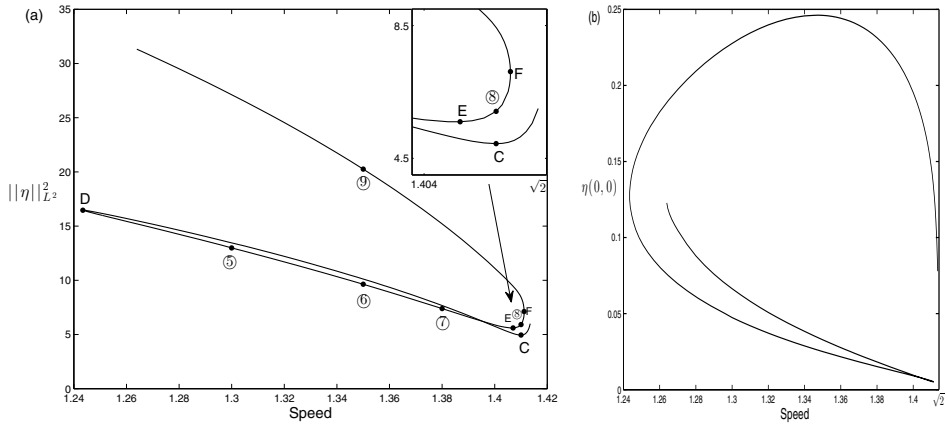

FIG. 6. (a) *Speed-energy bifurcation curve for* $2D$ *elevation solitary waves with the turning points* D *and* F *and the local minima* C *and* E. *The curve starts from the bifurcation point* $c = \sqrt{2}$, *then follows the path* C→D→⑤→⑥→⑦→E→⑧→F→⑨. *The portion close to the bifurcation point is shown in detail.* (b) *Values of* $\eta(0,0)$ *versus speed for the branch of* $2D$ *elevation solitary waves.*

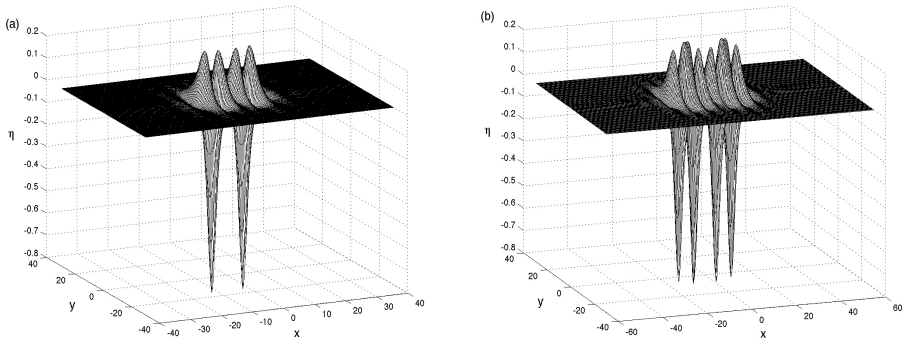

FIG. 7. *Typical profiles of elevation lumps for* (a) $c = 1.35$, $\eta(0,0) = 0.0251$, $||\eta||^2_{L^2} = 9.6288$ *(point labeled ⑥ in Figure* 6(a)*);* (b) $c = 1.35$, $\eta(0,0) = 0.0328$, $||\eta||^2_{L^2} = 20.2528$ *(point labeled ⑨ in Figure* 6(a)*).*

The analytical (Groves, Haragus, and Sun [10]) and the numerical (Milewski and Wang [19]) works, motivated by the transverse instability of plane solitary waves, offer another bifurcation mechanism for lump solutions. The authors in [10] and [19] pointed out that there is a family of traveling waves which are fully localized in the direction of propagation and nontrivially periodic in the spanwise direction which can bridge plane solitary waves and lumps. This family of solutions degenerates to a plane solitary wave as the period in the spanwise direction decreases to a nonzero critical value and becomes a lump as the period tends to be infinity. We show that this assertion is also true for the multilump elevation waves. Figure 8 shows the evolution from a plane solitary wave to a fully localized multilump solution as the period in the spanwise direction increases and the speed is fixed ($c = 1.38$).

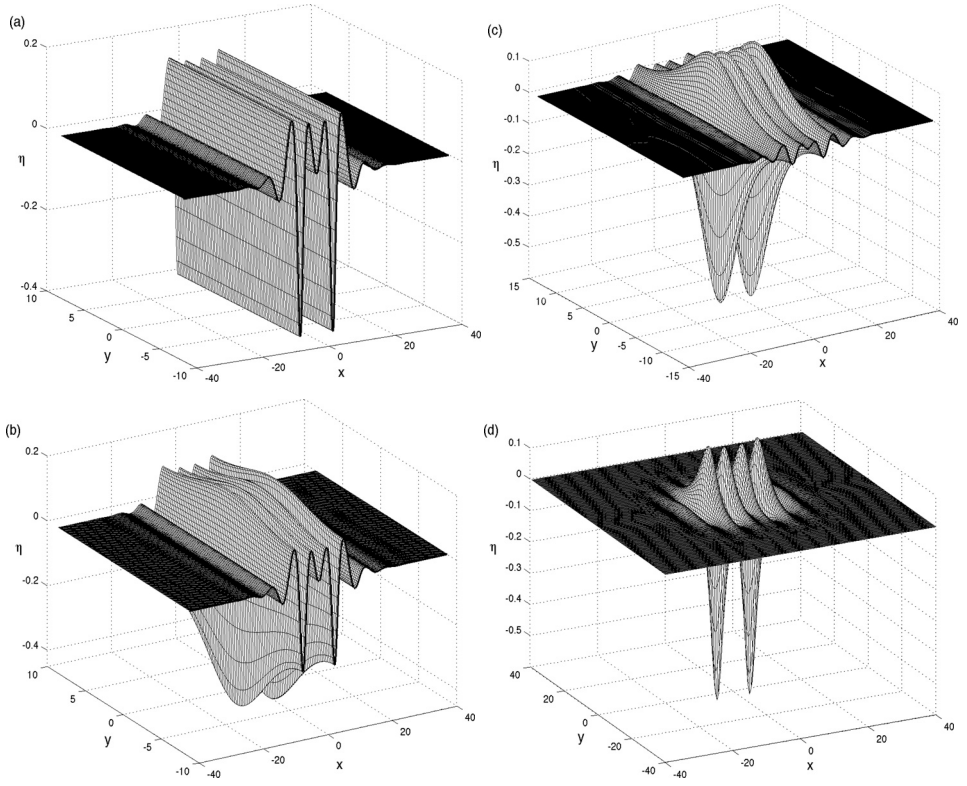

FIG. 8. *The formation of a symmetric multilump solitary wave via a secondary bifurcation of a plane solitary wave. A new family of traveling waves, which are fully localized in the propagation direction and nontrivially periodic in the transverse direction, branches off from the plane solitary wave* (a) *when the wavenumber in the transverse direction* $\beta_c \approx 0.38$. *Typical profiles of the transversally periodic solitary waves are shown in* (b) *and* (c) *corresponding to* $\beta = 0.3590$ *and* $\beta = 0.2285$, *respectively. Finally, as* $\beta \downarrow 0$, *a fully localized multilump solution* (d), *which corresponds to the point* ⑦ *in Figure* 6, *forms.*

We now take a plane solitary wave solution $U(\theta)$ and perturb it with a cosinus wave. Substituting the ansatz $\eta = U(\theta) + \epsilon\widetilde{\eta}(\theta)\cos(\beta y)$ into system (2.17) and linearizing it with respect to the perturbation parameter ϵ, we obtain

$$\left[\left(\frac{\sqrt{2}}{2} - c\right)\partial_\theta + \frac{\sqrt{2}}{4}\mathcal{H}\partial_{\theta\theta} + \frac{\sqrt{11}}{4}U_\theta + \frac{\sqrt{11}}{4}U\partial_\theta\right]\widetilde{\eta} = \frac{\sqrt{2}}{4}\left(1 + 2\beta^2\right)\mathcal{H}[\widetilde{\eta}] \tag{3.14}$$

with the boundary condition $\widetilde{\eta} \to 0$ as $\theta \to \pm\infty$. The threshold wavenumber for the new branch leading to the lump solution is obtained by picking the maximal positive β. The critical value of β for the example (Figure 8) is 0.379. This was obtained by solving numerically the eigenvalue problem (3.14). This theoretical prediction is in agreement with the numerical result (≈ 0.38) as shown in Figure 8(a).

The finding of the 1D nonsymmetric gravity-capillary solitary waves inspires us to generalize the result to the 2D case. For simplicity, we assume that the solutions are symmetric in the spanwise direction (i.e., $\eta(x, -y) = \eta(x, y)$), but nonsymmetric in the wave propagation direction (namely, $\eta(x_0 - x, y) \not\equiv \eta(x + x_0, y)$ for arbitrary x_0). The loss of the symmetry in one direction requires doubling the number of unknowns in

the numerics, but we still use at least 400×100 grid points along the wave propagation and spanwise directions, respectively. In order to find a nonsymmetric lump, it is essential to choose a good initial guess for the Newton's method. We prepare the initial data by gluing successively a depression lump and an elevation lump along the x-axis, both of which travel with the same speed. The Newton's method can then produce a new solitary-wave solution without symmetry in the x-direction. Once this solution is obtained, a global investigation of the nonsymmetric solutions along this branch can be carried out through numerical continuation methods.

The speed-energy bifurcation diagram of a branch of nonsymmetric lumps is shown in Figure 9. The 2D nonsymmetric solitary waves (solid line), which decay in both the x- and y-directions, appear via a spontaneous symmetry-breaking bifurcation. The bifurcation curve then experiences a turning point at $c \approx 1.3388$, where the wave speed attains its minimum, and finally terminates on another symmetry-breaking bifurcation. It is worth mentioning that the symmetric branches (dashed lines in Figure 9), from which the nonsymmetric solutions bifurcate, also show turning points on the speed-energy curves, and the nonsymmetric branch intersects the symmetric branches near these turning points.

Typical profiles of nonsymmetric lumps corresponding to the points ⑫ and ⑩ in Figure 9 are shown in Figure 10(a) and Figure 11(d) with their centerline profiles (Figure 10(b)). The profiles show a multilump structure. Figure 10(b) shows the comparison of the centerline profiles of two solutions propagating with the same speed $c = 1.4$. The two profiles are almost the same from the vertical dashed line to the right end but differ abruptly on the left parts.

The existence of nonsymmetric multilump solutions can also be interpreted as a secondary bifurcation, and one example is given in Figure 11. A new branch of traveling-wave solutions which feature nontrivial periodic variations in the spanwise direction bifurcates from a nonsymmetric plane solitary wave (Figure 11(a)). The bifurcation wavenumber is $\beta \approx 0.25$, which is coincident with the prediction (≈ 0.247) of (3.14). As the period in the spanwise direction increases, the profile becomes more and more localized and approaches a nonsymmetric multilump solution (Figures 11(b)–(d)). It is worth mentioning that the eigenvalue problem (3.14) is solved by using ARPACK in MATLAB, since the matrix is non-Hermitian due to the nonsymmetric nature of the plane wave. It is finally noted that so far we were not able to find the solutions which are nonsymmetric along the spanwise direction.

3.4. Stability of multilump solitary waves. As for the transverse instability of plane solitary waves, the quantity $\frac{\mathrm{d}}{\mathrm{d}c}\big|\big|\eta\big|\big|_{L^2}^2$ plays an important role in the stability characteristics of lumps. The argument proceeds in the same vein. $\rho(\theta, y; c)$ is supposed to be a locally confined traveling-wave solution propagating in the x-direction with the speed c and perturbed by $\epsilon\widetilde{\rho}(\theta, y; c)e^{\lambda t}$, where ϵ is a small parameter. By substituting this ansatz into (2.11) and collecting the coefficient of $e^{\lambda t}$, we obtain the linearized equation

$$\left(\frac{\sqrt{2}}{2} - c\right)\widetilde{\rho}_\theta - \frac{\sqrt{2}}{4}\mathcal{H}\Big[\widetilde{\rho} - \widetilde{\rho}_{\theta\theta} - 2\widetilde{\rho}_{yy}\Big] + \frac{\sqrt{11}}{4}\Big(\rho\widetilde{\rho}\Big)_\theta = -\lambda\widetilde{\rho}\,. \tag{3.15}$$

Expanding $\widetilde{\rho}$ as Taylor series in terms of the small parameter λ

$$\widetilde{\rho} = \rho^{(0)} + \lambda\rho^{(1)} + \lambda^2\rho^{(2)} + \cdots \tag{3.16}$$

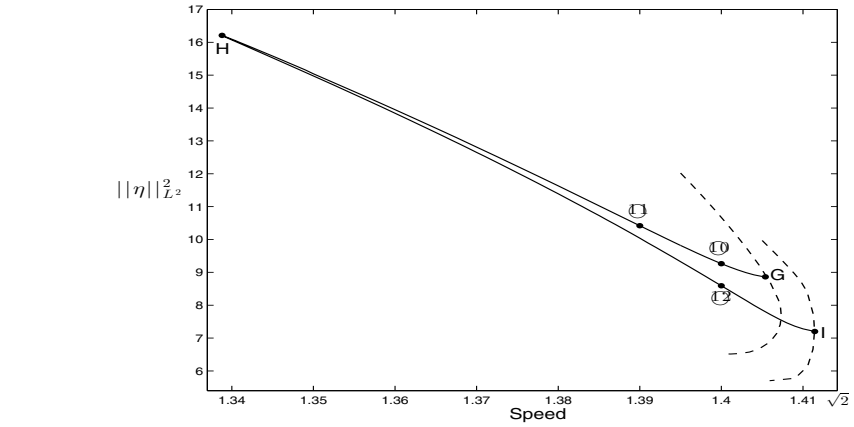

FIG. 9. *The speed-energy bifurcation curve of a branch of nonsymmetric multilump solitary waves (solid line) with a sharp turning point H at* $c = 1.3388$. *These waves appear via spontaneous symmetry-breaking bifurcations at the points* G *and* I, *and the associated branches of symmetric multilump solutions are shown by dashed curves.*

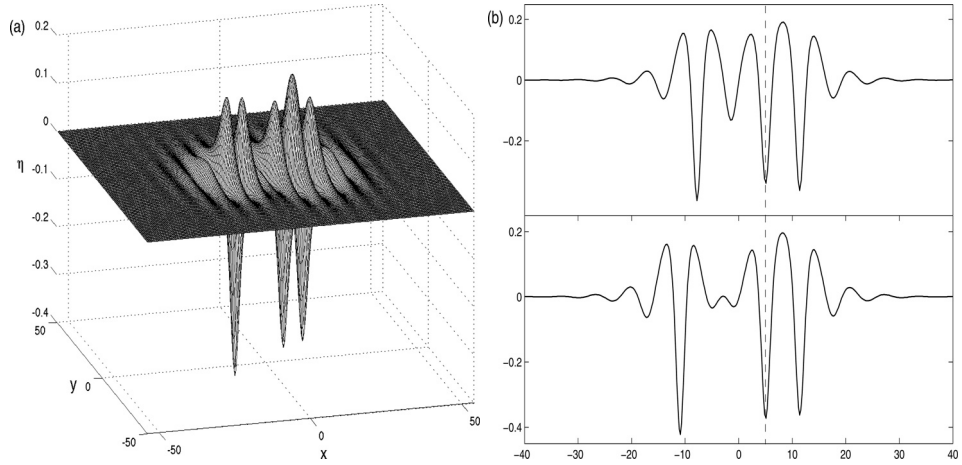

FIG. 10. (a) *A typical profile of nonsymmetric multilump solitary waves (labeled* ⑫ *in Figure* 9*).* (b) *The comparison of the centerline profile* $\eta(x, 0)$ *for different nonsymmetric lumps propagating at the same speed* ($c = 1.4$). *The upper plot corresponds to the solution labeled* ⑩ *in Figure* 9, *and the bottom plot corresponds to point* ⑫.

and substituting into (3.15) gives $\rho^{(0)} = \rho_\theta$ and $\rho^{(1)} = -\rho_c$ by using an argument similar to that outlined in section 3.2. Subsequently collecting terms of $O(\lambda^2)$ gives the equation for $\rho^{(2)}$,

$$\left(\frac{\sqrt{2}}{2} - c\right)\rho^{(2)} - \frac{\sqrt{2}}{4}\mathcal{H}\left[\rho^{(2)} - \rho^{(2)}_{\theta\theta} - 2\rho^{(2)}_{yy}\right] + \frac{\sqrt{11}}{4}\left(\rho\rho^{(2)}\right)_\theta = \rho_c\,. \tag{3.17}$$

Therefore the solvability condition

$$\int\int_{\mathbb{R}^2} \rho\rho_c \, d\theta dy = \frac{1}{2}\frac{\mathrm{d}}{\mathrm{dc}}\int\int_{\mathbb{R}^2} \rho^2 \, d\theta dy = 0 \tag{3.18}$$

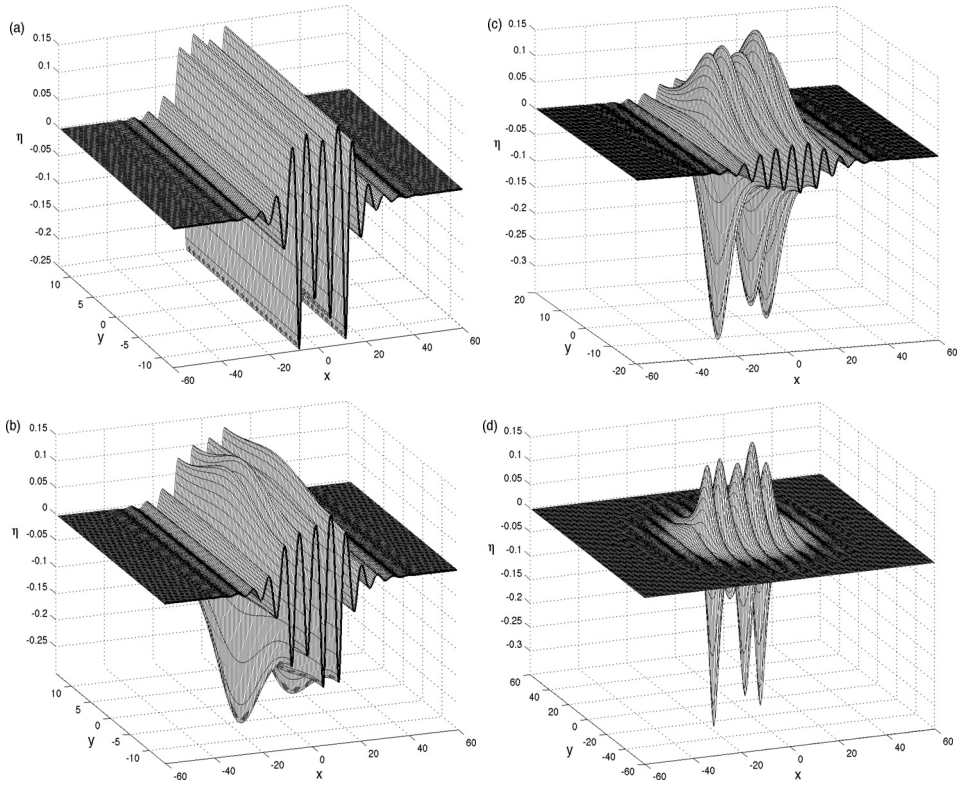

FIG. 11. *The formation of a nonsymmetric multilump solitary wave via a secondary bifurcation of a nonsymmetric plane solitary wave.* (a) *The bifurcation appears at* $\beta_c \approx 0.25$. *Typical profiles of the transversally periodic solitary waves are shown in* (b) *and* (c), *corresponding to* $\beta = 0.2185$ *and* $\beta = 0.1571$, *respectively. Finally, as* $\beta \downarrow 0$, *it converges to a fully localized, nonsymmetric and multilump solution* (d) *(corresponding to point* ⑩ *in Figure* 9*).*

gives us the necessary condition that the translational eigenmode becomes unstable only if the L^2-norm of the lump is at a local extremum when viewed as a function of the translating speed. Figure 6(a) implies that the stability characteristics of the elevation branch may change at C and E (critical points) and at D and F(turning points). It is noted that based on the reduced model the stability of the single-hump elevation lumps has already been studied by Akers and Milewski [1], who numerically showed that elevation lumps are unstable before point D.

We take the point ⑤ in Figure 6(a) as a typical example to show that waves between points D and E are unstable (see Figure 12). The initial profile which consists of two depression lumps (similar to Figure 7(a)) is perturbed by numerical noise. Unlike 1D stable elevation waves (see Figure 3), the spanwise direction adds freedom for triggering the instability in two dimensions. The decoupling of two depression lumps happens in the spanwise direction, which starts to be visible in (b) and is fully completed in (d).

We then consider the stability characteristics between E and F in Figure 6(a), a segment close to the bifurcation point. The authors in [1, 22] showed that small-amplitude single-lump elevation waves (corresponding to the portion before C in

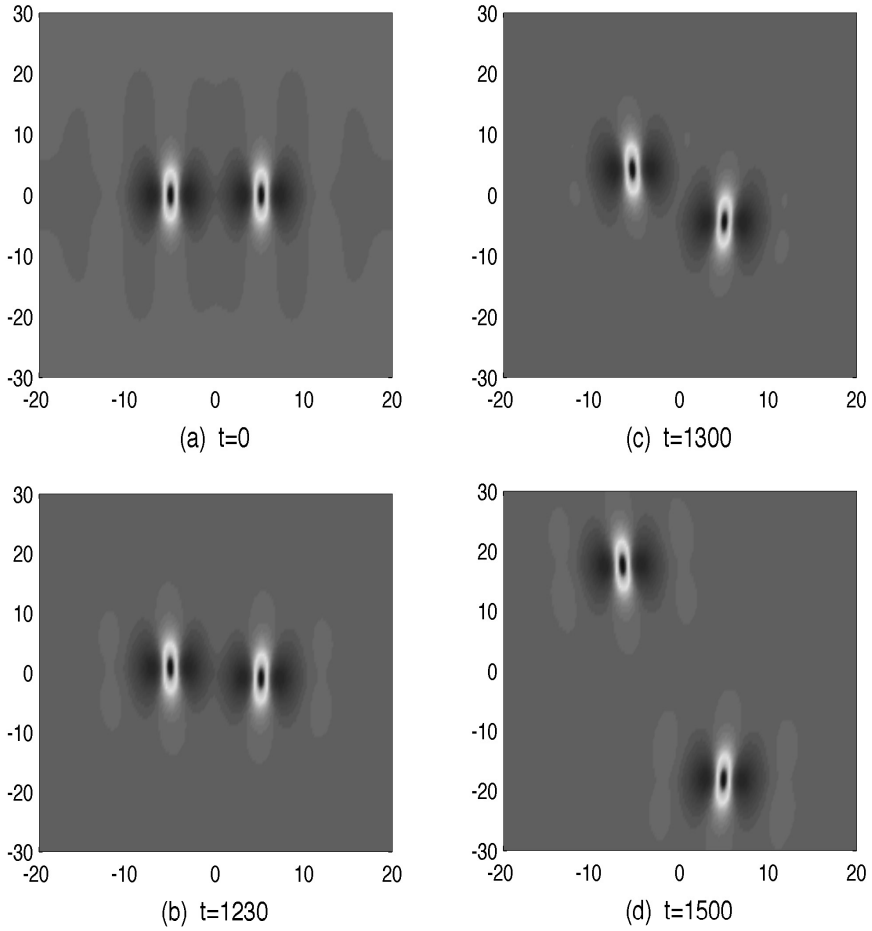

FIG. 12. *Four snapshots of the evolution of a symmetric multilump elevation wave with* $c = 1.3$ *and* $\eta(0,0) = 0.0474$ *(labeled* ⑤ *in Figure* 6(a)*). The undisturbed steady solution is similar to Figure* 7(a)*. The numerical noise can cause two main depression lumps to decouple in the transverse direction. The solution is shown at* $t = 1230$*, when the initial instability starts to be visible, and then* $t = 1300$*, when the apparent separation shows up.*

Figure 6(a)) disperse out for negative energy perturbations but focus and evolve into an oscillatory state of depression lumps for positive energy perturbations. However, small-amplitude multilump elevation waves have different dynamical behaviors of instability. An example of this is shown in Figure 13, where we track the maximum amplitude of the free surface arising from perturbed initial data. For a positive energy perturbation, there is an initial focusing instability resulting in large growth. What follows is a decrease of the amplitude (solid curve in Figure 13(b)), and the free surface finally decays into dispersive waves. This is to be contrasted to the single-hump solutions, which are stopped by the formation of a recurrent finite-amplitude oscillatory depression state.

There are single-hump elevation components in the symmetric solutions after point F in Figure 6(a) and in the nonsymmetric solutions presented in Figure 9.

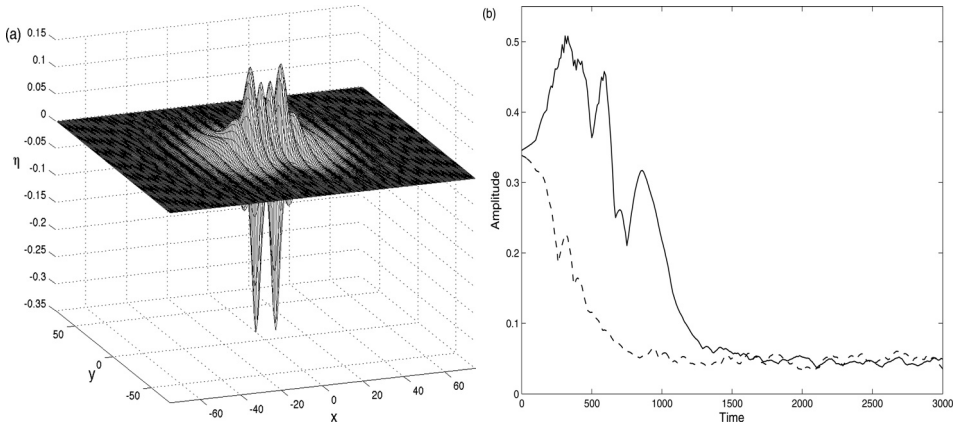

FIG. 13. *Instability of solitary waves between* E *and* F *in Figure* 6(a). *A symmetric multilump elevation wave with* $c = 1.41$ *and* $\eta(0,0) = 0.0058$ *(shown in* (a)*) was subjected to the* 1% *positive energy perturbation (solid curve) and* 1% *negative energy perturbation (dashed curve). The solution finally disperses out regardless of the perturbation.*

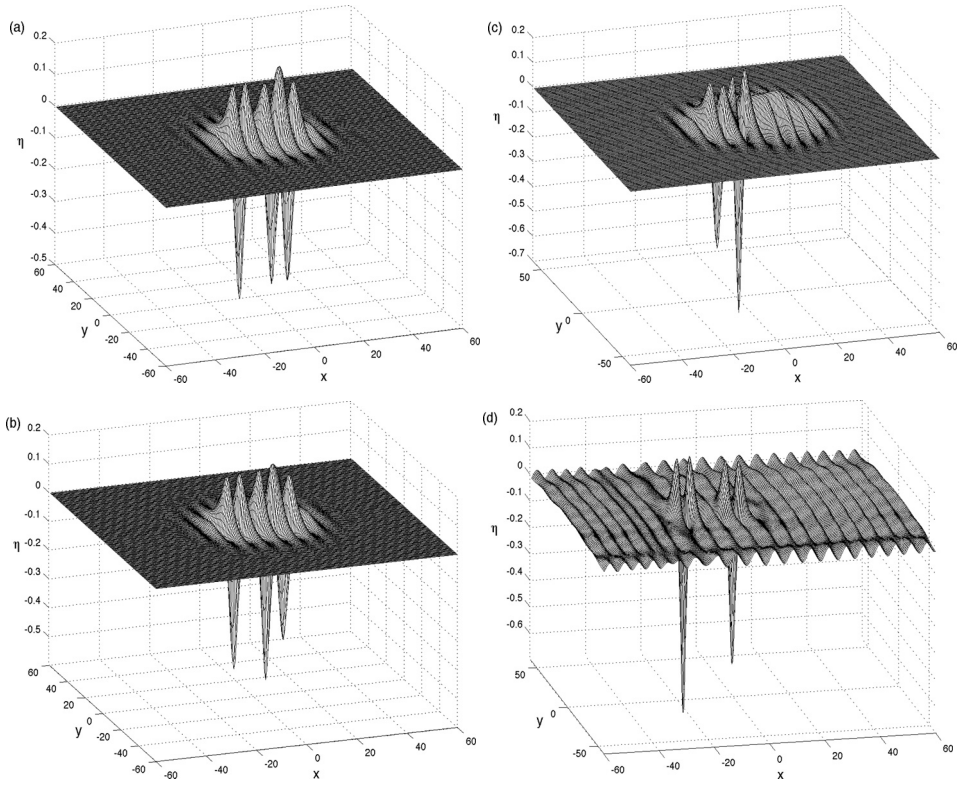

FIG. 14. *Snapshots of the evolution of a nonsymmetric solitary wave with* $c = 1.39$ *(corresponding to point* U *in Figure* 9*) in the model equation at* (a) $t = 0$, (b) $t = 600$, (c) $t = 700$, (d) $t = 1000$. *The perturbation is the numerical noise, and the unstable wave evolves into two breathers and small-amplitude waves radiated during the instability.*

Therefore we expect the symmetry-breaking instability for the elevation component, which eventually leads to the formation of multiple depression lumps with different amplitudes. An illustrative example for the evolution of a nonsymmetric multilump solution is shown in Figure 14.

4. Conclusion. It is well known that the gravity-capillary free-surface flows support a very rich structure of solitary-wave solutions. The recent findings of the snakelike pattern of the symmetric elevation branch in bifurcation and the existence of the nonsymmetric solitary waves in the 1D problem initiated our study. Here, based on a reduced model proposed by Akers and Milewski [1], we generalized the results to the 2D case. The bifurcation curves of the 2D symmetric elevation lumps were traced via a numerical continuation method to pass through several turning points. Lumps, which are nonsymmetric along the wave propagation direction, were computed numerically and found to appear via spontaneous symmetry-breaking bifurcations. Both of them feature a multilump structure and can be viewed as bifurcating along a new family of traveling-wave solutions which are fully localized in the propagation direction and nontrivially periodic in the spanwise direction. The discovery of these multilump solutions in the model equation leads us to postulate the existence of similar solutions in the full Euler equations in deep water.

The instability and subsequent evolution of 1D multimodal plane solitary waves and of 2D multilump solitary waves have been explored numerically by perturbing the waves and computing the solution by integrating in time the model equation. All the solitary waves that we computed in this paper were found to be unstable, and their dynamical behaviors turned out to be very different from those of the single-lump solutions.

Appendix A. Numerical method for 1D steady waves for the full Euler equations. In this appendix, the detailed numerical formulation is presented for computing 1D steady gravity-capillary waves propagating in deep water. The formulation is based on the hodograph transformation and the Cauchy integral formula. This numerical scheme was originated from the work of Vanden-Broeck and Dias [20] and later used in a few papers (for example, [2, 8, 13]).

Since we seek fully localized waves traveling with the translating speed c for (2.1), (2.2), (2.5), and (2.6), we choose a frame of reference moving with the same speed. We define $\theta = x + ct$ and introduce a new function $\widehat{\phi}(\theta, z) = \phi + c\theta$. Therefore the kinematic and dynamic boundary conditions read

$$\begin{cases} \widehat{\phi}_\theta \, \eta_\theta = \widehat{\phi}_z \,, \\ \dfrac{1}{2}\left(\widehat{\phi}_\theta^2 + \widehat{\phi}_z^2 - c^2\right) + \eta - \dfrac{\eta_{\theta\theta}}{(1+\eta_\theta^2)^{3/2}} = 0 \,. \end{cases} \tag{A.1}$$

We introduce the complex potential

$$f(w) = \widehat{\phi} + i\psi, \tag{A.2}$$

where ψ is the stream function and $w = \theta + iz$. We use a hodograph transformation to exchange the dependent and independent variables:

$$w(f) = \theta(f) + iz(f) \,. \tag{A.3}$$

It follows immediately that

$$\widehat{\phi}_\theta - i\widehat{\phi}_z = \frac{df}{dw} = \frac{1}{\theta_{\widehat{\phi}} + iz_{\widehat{\phi}}} \,. \tag{A.4}$$

Without loss of generality we choose $\theta = 0$ at $\widehat{\phi} = 0$ and $\psi = 0$ for the free surface. Applying the Cauchy integral formula to the fluid layer yields

$$\dot{\Theta}\left(\widehat{\phi}\right) = \frac{1}{c} + \frac{1}{\pi}\int_{\mathbb{R}} \frac{\dot{Z}\left(\widehat{\phi}'\right)}{\widehat{\phi} - \widehat{\phi}'}\, d\widehat{\phi}', \tag{A.5}$$

where $\Theta(\widehat{\phi}) = \theta(\widehat{\phi} + i\,0)$ and $Z(\widehat{\phi}) = z(\widehat{\phi} + i\,0)$. Furthermore, the dynamic boundary condition in the inverse plane takes the form

$$\frac{1}{2}\left(\frac{1}{\dot{\Theta}^2 + \dot{Z}^2} - c^2\right) + Z + \frac{\ddot{\Theta}\dot{Z} - \ddot{Z}\dot{\Theta}}{\left(\dot{\Theta}^2 + \dot{Z}^2\right)^{3/2}} = 0\,. \tag{A.6}$$

It is obvious that (A.5) is nearly singular as c approaches zero. To overcome this difficulty, we redefine $\widehat{\phi} = c\xi$. After some algebra, (A.5) and (A.6) can be recast as

$$\begin{cases} \dot{\Theta}(\xi) = 1 + \dfrac{1}{\pi}\displaystyle\int_{\mathbb{R}} \frac{\dot{Z}(\xi')}{\xi - \xi'}\, d\xi' = 1 + \mathcal{H}\left[\dot{Z}\right], \\ \dfrac{c^2}{2}\left(\dfrac{1}{\dot{\Theta}^2 + \dot{Z}^2} - 1\right) + Z + \dfrac{\ddot{\Theta}\dot{Z} - \ddot{Z}\dot{\Theta}}{\left(\dot{\Theta}^2 + \dot{Z}^2\right)^{3/2}} = 0\,. \end{cases} \tag{A.7}$$

And finally the energy (3.1) in the transformed plane can be written as

$$\mathcal{E} = \frac{c^2}{2}\int_{\mathbb{R}} Z\mathcal{H}[Z_\xi]\, d\xi + \frac{1}{2}\int_{\mathbb{R}} Z^2\dot{\Theta}\, d\xi + \int_{\mathbb{R}}\left(\sqrt{\dot{\Theta}^2 + \dot{Z}^2} - \dot{\Theta}\right) d\xi\,. \tag{A.8}$$

This agrees with the formula given in [18, 23].

Acknowledgment. The authors acknowledge fruitful discussions on the topic of this paper with Prof. Paul Milewski.

REFERENCES

[1] B. Akers and P. A. Milewski, *A model equation for wavepacket solitary waves arising from capillary-gravity flows*, Stud. Appl. Math., 122 (2009), pp. 249–274.

[2] D. C. Calvo and T. R. Akylas, *Stability of steep gravity-capillary waves in deep water*, J. Fluid Mech., 452 (2002), pp. 123–143.

[3] J. D. Diorio, Y. Cho, J. H. Duncan, and T. R. Akylas, *Gravity-capillary lumps generated by a moving pressure source*, Phys. Rev. Lett., 103 (2009), 214502.

[4] J. D. Diorio, Y. Cho, J. H. Duncan, and T. R. Akylas, *Resonantly forced gravity-capillary lumps on deep water. Part* 1. *Experiment*, J. Fluid Mech., 672 (2011), pp. 268–287.

[5] Y. Cho, J. D. Diorio, T. R. Akylas, and J. H. Duncan, *Resonantly forced gravity-capillary lumps on deep water. Part* 2. *Theoretical model*, J. Fluid Mech., 672 (2011), pp. 288–306.

[6] W. Craig, *Non-existence of solitary water waves in three dimensions*, Phil. Trans. R. Soc. Lond. A, 360 (2002), pp. 2127–2135.

[7] F. Dias and G. Iooss, *Capillary-gravity solitary waves with damped oscillations*, Physica D, 65 (1993), pp. 399–423.

[8] F. Dias, D. Menasce, and J.-M. Vanden-Broeck, *Numerical study of capillary-gravity solitary waves*, Eur. J. Mech. B: Fluids, 15 (1996), pp. 17–36.

[9] L. Falcon, C. Laroche, and S. Fauve, *Observation of gravitycapillary wave turbulence*, Phys. Rev. Lett., 98 (2007), pp. 094503.

[10] M. D. Groves, M. Haragus, and S. M. Sun, *A dimension-breaking phenomenon in the theory of steady gravity-capillary water waves*, Philos. Trans. R. Soc. Lond. Ser. A, 360 (2002), pp. 2189–2243.

[11] M. S. Longuet-Higgins, *Limiting forms for capillary-gravity waves*, J. Fluid Mech., 194 (1988), pp. 351–375.
[12] M. S. Longuet-Higgins, *Capillary-gravity waves of solitary type on deep water*, J. Fluid Mech., 200 (1989), pp. 451–478.
[13] B. Kim and T. R. Akylas, *On gravity-capillary lumps*, J. Fluid Mech., 540 (2005), pp. 337–351.
[14] B. Kim and T. R. Akylas, *Transverse instability of gravity-capillary solitary waves*, J. Engrg. Math., 58 (2007), pp. 167–175.
[15] E. I. Părău, J.-M. Vanden-Broeck, and M. J. Cooker, *Nonlinear three-dimensional gravity-capillary solitary waves*, J. Fluid Mech., 536 (2005), pp. 99–105.
[16] C. C. Mei, *The Applied Dynamics of Ocean Surface Waves*, Wiley, New York, 1983.
[17] P. A. Milewski, *Three-dimensional localized gravity-capillary waves*, Comm. Math. Sci., 3 (2005), pp. 89–99.
[18] P. A. Milewski, J.-M. Vanden-Broeck, and Z. Wang, *Dynamics of steep two-dimensional gravity-capillary solitary waves*, J. Fluid Mech., 664 (2010), pp. 466–477.
[19] P. A. Milewski and Z. Wang, *Transversally periodic solitary gravity-capillary waves*, Proc. R. Soc. Lond. Ser. A Math. Phys. Eng. Sci., 470 (2014), 20130537.
[20] J.-M. Vanden-Broeck and F. Dias, *Gravity-capillary solitary waves in water of infinite depth and related free-surface flows*, J. Fluid Mech., 240 (1992), pp. 549–557.
[21] A. H. Schooley, *Profiles of wind-created water waves in the capillary-gravity transition region*, J. Mar. Res., 16 (1958), pp. 100–108.
[22] Z. Wang and P. A. Milewski, *Dynamics of gravity-capillary solitary waves in deep water*, J. Fluid Mech., 708 (2012), pp. 480–501.
[23] Z. Wang, J.-M. Vanden-Broeck, and P. A. Milewski, *Asymmetric gravity-capillary solitary waves on deep water*, J. Fluid Mech., 759 (2014).
[24] J. W. Wright, *Detection of ocean waves by microwave radar: The modulation of short gravity-capillary waves*, Boundary-Layer Meteorol., 13 (1978), pp. 87–105.
[25] T. S. Yang and T. R. Akylas, *On asymmetric gravity-capillary solitary waves*, J. Fluid Mech., 330 (1997), pp. 215–232.
[26] X. Zhang, *Capillary-gravity and capillary waves generated in a wind wave tank: Observations and theories*, J. Fluid Mech., 289 (1995), pp. 51–82.
[27] J. A. Zufiria, *Symmetry breaking in periodic and solitary gravity-capillary waves on water of finite depth*, J. Fluid Mech., 184 (1987), pp. 183–206.